Single-Voxel MR Spectroscopy

Geoffrey S. Payne

The Institute of Cancer Research and Royal Marsden Hospital, Surrey, UK

The most widely used single-voxel spectroscopy methods are called PRESS (point-resolved spectroscopy), ISIS (image-selected in vivo spectroscopy), and STEAM (stimulated echo acquisition mode). They were developed in the 1980s for the selection of magnetic resonance spectroscopy signals from a single voxel. PRESS and STEAM enable single-shot acquisition, while ISIS requires an appropriate addition and subtraction of eight measurements to localize signals in three dimensions. This article describes these methods, subsequent developments (for example, use with adiabatic radiofrequency pulses), and their relative merits for different applications. The more recently developed localization by adiabatic selective refocusing sequence is also described, together with a discussion of several practical considerations such as slice profile effects, the chemical shift displacement artifact, shimming, water and fat suppression, temporal frequency changes, and subject motion.

Keywords: single-voxel spectroscopy, PRESS, STEAM, ISIS, LASER, chemical shift displacement artifact, motion

How to cite this article:
eMagRes, 2015, Vol 4: 709–720. DOI 10.1002/9780470034590.emrstm1483

Introduction

Acquiring spectral data from a single target voxel is particularly useful when a lesion has been identified using other magnetic resonance (MR) imaging methods, and the biochemical information contained in an MR spectrum may supply useful additional information for differential diagnosis and evaluation. Single-voxel methods are also helpful when time is limited as they generally only require a single acquisition, or eight for the image-selected in vivo spectroscopy (ISIS) technique, to achieve localization. This permits a more flexible trading between voxel size and total scan time than is possible with spectroscopic imaging. The single-shot nature of point-resolved spectroscopy (PRESS) and stimulated echo acquisition mode (STEAM) also makes them more attractive for use in the presence of motion. They have the appearance of simplicity, and indeed single-voxel spectra are much simpler to acquire and evaluate than multivoxel spectroscopic imaging data. However, in addition to there being a variety of basic acquisition strategies, there are a number of issues that need to be understood for optimal acquisition and interpretation of the results. In this article the most widely used acquisition strategies are described, followed by a discussion of issues related to data acquisition and processing that are common to many of them.

Single-Voxel Localization Methods

In the early years of magnetic resonance spectroscopy (MRS), in vivo localization was achieved by relying on the sensitivity profile of radiofrequency (RF) transmit/receive surface coils.[1] This method was only suitable for surface tissues. For deeper regions, the method of topical MR made use of the inhomogeneity of the magnetic field surrounding a single sweet spot of homogeneous field to create spectra with sharp resonance lines from the central region only.[2] Both these methods had many limitations, including very poorly defined boundaries. For many applications, the intense RF fields close to the coil led to strong contaminating signals from superficial tissues such as muscles. One of the first uses of localizing spectroscopy using slice selection was the depth-resolved surface coil spectroscopy (DRESS[3]) technique, in which a frequency-selective excitation pulse was played out in the presence of a magnetic field gradient, to select a slice parallel to the surface coil. This method selected signal from a disc-shaped region, for which the thickness and position were determined by the slice selection and the diameter by the sensitivity profile of the RF coil.

In the mid-1980s, several localization strategies were developed that used the intersection of selected slices (excited using frequency-selective RF pulses in combination with magnetic field gradients) to localize MRS signals to a target cuboid region. Three of these strategies quickly became recognized as the most useful, PRESS, STEAM, and ISIS, and are commonly implemented on clinical MRI systems. Usually, the target region is a cuboid, but this is not necessarily so as the slices do not need to be orthogonal to each other. They have an increasingly well-defined slice profile, and are readily positioned using MR images acquired in the same session using a graphical user interface. These methods are described below. The LASER (localization by adiabatic selective refocusing) sequence is also described. This is a relatively recent modification of the PRESS sequence suitable for use with inhomogeneous RF fields. As all these methods depend on slice profile effects, a brief discussion of these is given first.

Slice Selection and Slice Profiles

All the single-voxel localization sequences use a series of slice-selective pulses to localize signal to a cuboid or parallelepiped. Slice selection is achieved by playing out a frequency-selective RF pulse in the presence of a magnetic field gradient. The slice thickness (SL) is determined by the bandwidth of the RF pulse (BW), the strength of the magnetic field gradient (G), and the gyromagnetic ratio of the nucleus according to equation (1).

$$\text{SL (mm)} = \text{BW (Hz)}/[\gamma\text{(MHz/T)} \cdot \text{G (mT/m)}] \quad (1)$$

During slice-selective RF pulses, transverse magnetization is dephased by the gradient as a function of position across the slice. For 180-degree inversion or refocusing RF pulses the spin phase is also inverted by the RF pulse itself, so that this dephasing is rephased during the 2nd part of the pulse. However to refocus the spins following slice-selective excitation pulses it is necessary to append a reversed gradient pulse which has an integral equal to the that of the slice-selection gradient from the center of the RF pulse to the end of the gradient pulse (see also the first pulse in the PRESS sequence in Figure 4 discussed later). The signal which is refocused at the end of this negative refocusing lobe, is called a gradient refocused echo.

For conventional amplitude-modulated RF pulses (e.g., Hanning-filtered sin$c$ or sin$x$/x-modulated pulses), the excitation bandwidth is inversely proportional to the pulse length. To minimize off-resonance effects, and in particular, the chemical shift displacement artifact (see below), it is usually desirable to use the largest possible RF bandwidth, with a proportionally increased gradient amplitude to preserve SL (equation 1). As the flip angle is proportional to the area under the waveform, for a pulse of a given flip angle, higher pulse bandwidths lead to shorter pulses of higher peak amplitude. On most clinical MRI systems it is the maximum permitted voltage that can be applied to the RF transmitter coil that limits the maximum bandwidth for RF pulses of this type.

The slice profile is approximately given by the Fourier transform of the amplitude waveform. However, owing to the effects of nonlinearity (a 180° pulse does not give twice the signal of a 90° pulse, for example), this correspondence is only reasonable in the small tip-angle ($\leq$90°) regime. Pulse truncation is also a problem. To achieve a rectangular slice profile, a sin$c$ RF waveform is a good starting point. Figure 1(a) shows a two-cycle sin$c$ waveform (gray) with the corresponding calculated slice profile in Figure 1(b); there is clearly unwanted excitation outside of the main slice. Filters can be used to reduce the effects of truncation. The effect of the Hanning filter on the waveform and the resulting slice profile are also shown in Figure 1(a) and (b) (black); the result is reduced out-of-slice excitation at the expense of a wider transition region between full excitation and no excitation. It certainly does not display an ideal rectangular profile. More recently, numerical and recursive modeling has led to much improved pulse profiles for amplitude-modulated RF pulses, for example, those using the Shinnar–Le Roux algorithm,[4–6] and by Mao *et al.*[7] An example of a 90° pulse developed using the Shinnar–Le Roux algorithm is shown in Figure 1(c) and (d); at the expense of a slightly increased pulse length, the same amplitude RF ($B_1 = 9.4\,\mu$T or 400 Hz for hydrogen, ^{1}H, in this case) yields a much flatter profile with a much shorter transition region.

For 180° pulses, the slice profile of standard sin$c$ pulses deteriorates substantially (Figure 2a). However, because the purpose is slice-selective inversion and not the generation of

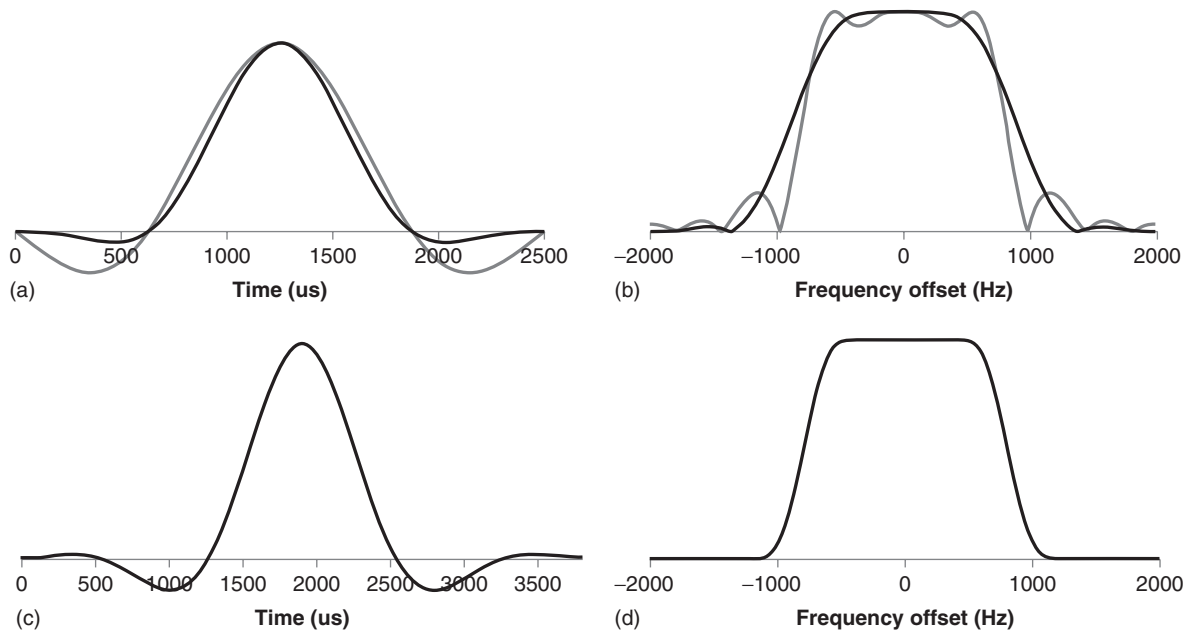

Figure 1. RF envelopes and resulting profiles for 90° pulses. (a) RF waveform for a two-cycle sin$c$ pulse (gray) and Hanning-filtered sin$c$ pulse (black). Amplitude 9.4 μT corresponding to 400 Hz for ^{1}H. (b) Corresponding calculated slice profiles of sin$c$ (gray) and Hanning-filtered sin$c$ (black). (c) RF envelope for 90° pulse calculated using the Shinnar–Le Roux algorithm. Amplitude 9.4 μT/400 Hz. (d) Corresponding calculated slice profile. The slice profiles were calculated using the Bloch routine in Bruker Topspin Software (v 3.2, Karlsruhe, Germany)

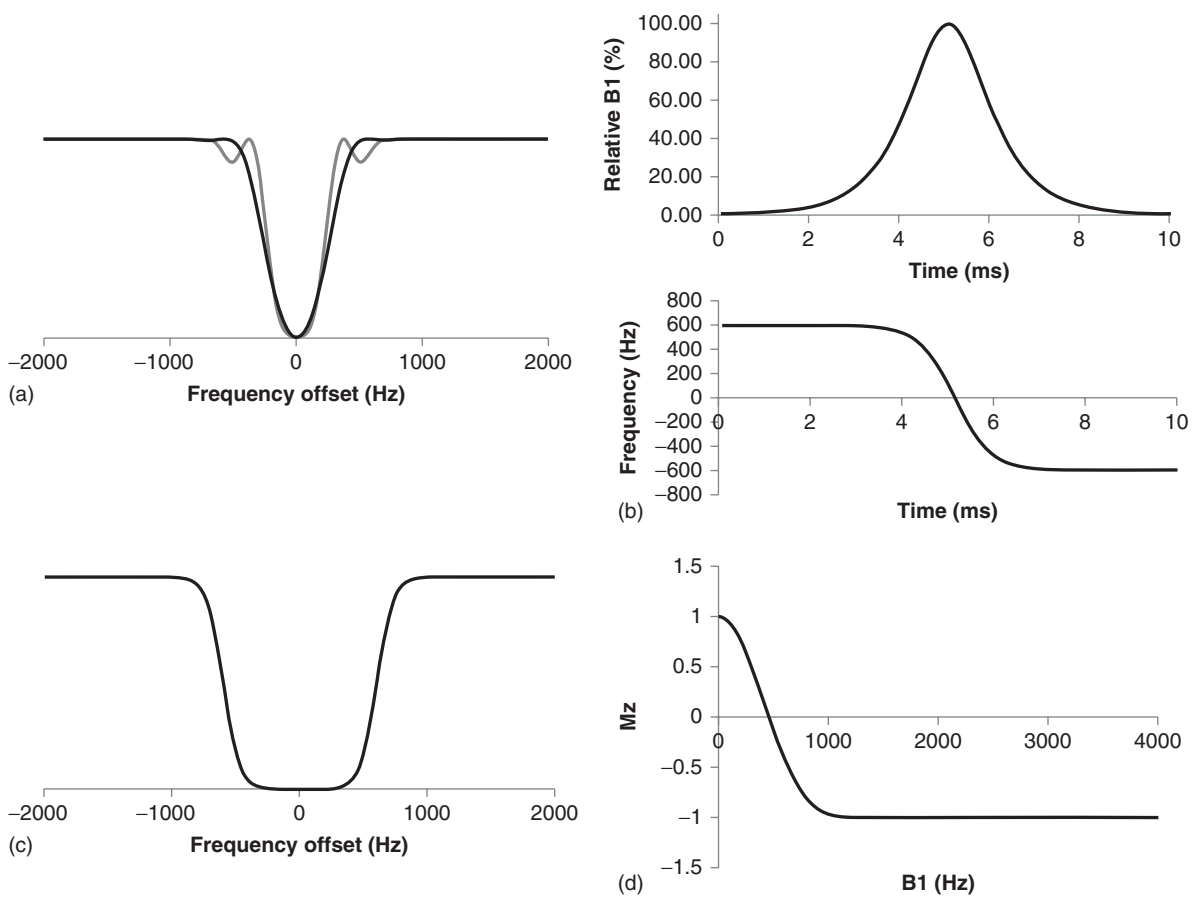

Figure 2. Inversion Pulses. (a) Calculated inversion profiles for two-cycle sinc pulse (grey curve) and two-cycle Hanning-filtered sinc pulse (amplitude 9.4 μT/400 Hz; duration 5 ms). (b) Amplitude and frequency sweep for a hyperbolic secant inversion pulse. (c) Corresponding inversion profile. (d) Dependence of Mz on RF amplitude, showing the threshold behavior characteristic of the hyperbolic secant pulse. The slice profiles were calculated using the Bloch routine in Bruker Topspin Software (v 3.2, Karlsruhe, Germany)

transverse magnetization, selective 180° pulses do not require negative refocusing gradients. Adiabatic RF pulses (see ***Adiabatic RF Pulses for MRS***), in which both amplitude and frequency (or phase) are modulated, have been demonstrated to produce much superior profiles for inversion. They were originally developed owing to their property that, above a certain threshold RF amplitude, their effect on a spin system or flip angle is independent of the RF amplitude. Figure 2(b) shows the RF amplitude and frequency waveforms for a widely used adiabatic inversion pulse, the hyperbolic secant pulse,[8,9] with the resulting inversion profile shown in Figure 2(c). This has a very attractive slice profile, with a flat central section, fairly sharp transition regions, and negligible out-of-slice ripple. Unfortunately, it is not possible to create a suitable adiabatic slice-selective excitation pulse. The threshold behavior is illustrated in Figure 2(d); unlike a standard amplitude-modulated pulse in which the magnetization continues to rotate about the B_1 field as the amplitude increases, here the magnetization rotates to the $-z$ axis and then stays there. This property makes them especially useful in combination with surface coil transmitters. Unfortunately, adiabatic inversion pulses are not good for slice-selective refocusing, owing to the resulting phase dispersion. However, a pair of identical adiabatic inversion pulses can achieve slice-selective refocusing. This combination is used in the LASER sequence (see below).

Chemical Shift Displacement Artifact

One particular feature associated with the use of slice selection is the Chemical Shift Displacement Artifact. This phenomenon is illustrated in Figure 3. For spins on resonance (e.g., water), the location and frequency f are related by $f(x) = \gamma \cdot G \cdot x$, analogous to equation (1). However, for spins chemically shifted with a frequency offset Δf, the relationship becomes $f(x) = \gamma \cdot G \cdot x + \Delta f$ (dashed line in Figure 3). A RF pulse with a given frequency range will therefore excite slightly different regions for the two species. The situation in Figure 3 is exaggerated for clarity but the effect is still significant; each spectral peak is localized to a voxel, which is slightly shifted relative to the voxels of the neighboring peaks.

For most purposes, it is the slice displacement relative to the size of the voxel that is important. This is given by Δf/BW. As an example, at 3 T, the frequency difference between water and fat in ^{1}H MRS is 3.4 ppm or about 434 Hz. If the RF bandwidth is 1200 Hz, then the 'fat' voxel is shifted by about 1/3 of the voxel

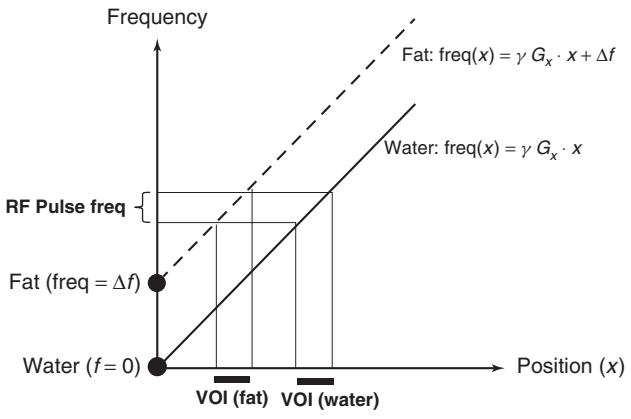

Figure 3. Illustration of Chemical Shift Displacement Artifact. For spins on resonance (e.g., water), the linear correspondence between frequency and position is determined by the Larmor equation, $\text{freq}(x) = \gamma\ G_x \cdot x$, where γ is the gyromagnetic ratio of the nucleus and G_x is the gradient strength in the x-direction. For a given set of frequencies in the RF pulse, this leads to excitation of the slice indicated by 'VOI (water)'. For spins at a relative frequency Δf, such as fat, there is still a linear relation between frequency and position, but it is offset by Δf, leading to slice selection at the position indicated by 'VOI (fat)'. The example illustrated is exaggerated for clarity, and the selected slices will normally overlap. However, for many MRS studies, the displacement between slices corresponding to different metabolites may well be of the order of 1/3 of the slice thickness

size relative to the water voxel. As this phenomenon occurs in each slice-select direction, the final overlap of tissue common to all voxels from different metabolites can be quite small. For a given chemical shift, Δf, the displacement artifact is minimized with the largest possible RF bandwidth with correspondingly high amplitude of the localizing gradient.

The chemical shift displacement artifact has several consequences. As mentioned above, it means that the signals from the metabolites of interest do not arise from exactly the same location. As most lesions of interest are heterogeneous, this can lead to misleading results. Most clinical MRI systems allow the user to specify the chemical shift offset that corresponds to the positioned voxel; it is usually best to shift this to somewhere in the middle of the spectrum. This strategy ensures that the actual voxel offset relative to that positioned on the image is kept to a minimum, however, it does not reduce the total offsets between the metabolites. Some scanners have the facility to show where the voxels really are for different chemically shifted species.

The second consequence is related to the first, in that it can affect the degree of contamination in a spectrum. For example, if a voxel is placed in the brain near the scalp, the ^{1}H MRS 'fat voxel' may include a contribution from scalp lipid that is not obvious from the voxel position. If one knows which way the 'fat voxel' has been shifted, it may be appropriate to reverse the gradient direction so that it is shifted away from the high-concentration lipid region.

The third consequence concerns coupled spin systems, such as lactate. Lactate is an AX_3 spin system in ^{1}H MRS, characterized by a $-CH_3$ doublet peak at 1.33 ppm and a $-CH$ quartet at 4.1 ppm. The 1.33 ppm doublet is the preferred resonance for measurement as it is larger, narrower, and is not affected by water suppression pulses at 4.7 ppm. The chemical shift displacement artifact causes the slices selected by excitation and refocusing pulses during volume selection to be spatially shifted for the $-CH$ quartet at 4.1 ppm relative to the $-CH_3$ doublet at 1.3 ppm. In the PRESS sequence, for example, this leads to some subvolumes of the total voxel experiencing a selective 180° RF pulse (affecting the $-CH_3$ doublet only, for example, which leads to refocusing of the doublet), while other subvolumes experience a nonselective 180° pulse, which does not lead to refocusing of the J-evolution (spin–spin coupling) of the spins. The different phase evolution leads to different relative phases in these regions and therefore overall partial signal cancellation.[10] This effect can be mitigated by expanding the nominal voxel size and then using saturation slices to eliminate the unwanted signals,[11] or by improving broadband RF pulse design,[12] or by use of FOCI (frequency offset corrected inversion),[13] VERSE (variable rate selective excitation),[14] or GOIA (gradient offset independent adiabaticity)[15] pulses to allow much larger bandwidth without increasing the peak RF amplitude (see under 'LASER' below).

PRESS

The PRESS sequence[16] is shown in Figure 4. Following initial slice selection, two frequency-selective refocusing RF pulses are played out in combination with gradient pulses. In general, these gradient pulses are along orthogonal axes, leading to signal from the intersection of the three slices being refocused, while signal from elsewhere is dephased. Additional crusher gradients are usually placed around the 180° refocus pulses to dephase signals excited by imperfections in the RF pulses. The minimum echo time (TE) available is determined by the length of the RF and gradient pulses, and on clinical MRI systems is usually about 30 ms. PRESS spectra are often acquired with a TE of 135 ms to yield an inverted absorption line shape for lactate and reduced signals from lipids and macromolecules. PRESS is also the most widely used single-voxel localization method to be combined with magnetic resonance spectroscopic imaging (MRSI) in order to restrict the field of view, e.g., to reduce lipid contamination from MRSI in the brain (see ***CSI and SENSE CSI***).

STEAM

The STEAM sequence[17] is shown in Figure 5. In many respects it closely resembles the PRESS sequence of Figure 4. However, instead of being a double full spin-echo sequence (90°–180°–180°), all the RF pulses have flip angles of 90°, leading to the final refocused signal being a stimulated echo rather than a spin echo. The main advantage of STEAM compared with PRESS is that the effective echo time can be shorter, leading to reduced losses from T_2 relaxation. The alignment of spins along $\pm z$, during the central 'TM' period helps with this as it does not contribute to TE. Historically, 90° RF pulses also had much better slice profiles than 180° pulses, which were very poor in early implementations of 180° refocus pulses (compare the slice profiles achieved with 90° Hanning-filtered sinc pulses in Figures 1 and 2). However, RF pulse shaping has improved very significantly and this is no longer such a significant issue. 90° RF pulses also require lower B_1 fields to

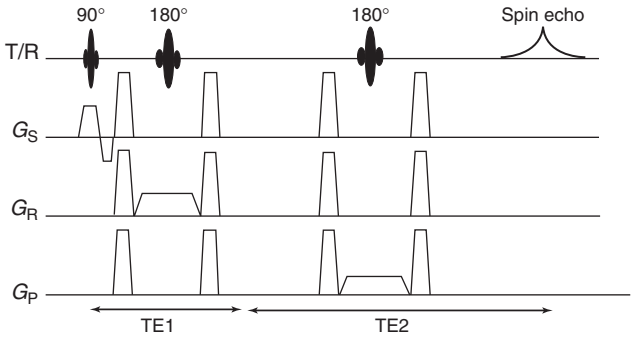

Figure 4. Timing diagram for PRESS. Strong spoiler gradients are placed around the 180° refocus pulses to avoid fresh magnetization excited by these pulses from contributing to the detected signal. Although the full echo signal is drawn, it is usually very asymmetric, with the second half very much longer than the first half. For most purposes, only the second half is acquired, effectively as an FID. T/R indicates radiofrequency transmit pulses and received signal; G_S, G_R, and G_P are gradients in the slice, read, and phase-encode directions, respectively with a negative gradient refocusing lobe on G_S; and TE1 and TE2 are the echo times corresponding to the two refocusing 180° RF pulses, with the total echo time being given by TE1 + TE2

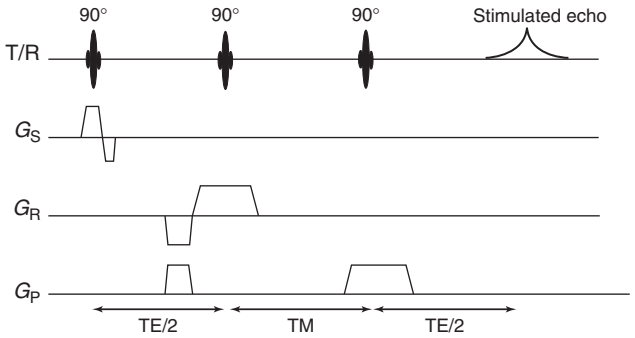

Figure 5. STEAM Sequence. T/R indicates radiofrequency transmit pulses and received signal; G_S, G_R, and G_P are gradients in the slice, read, and phase-encode directions, respectively; and TE is the total echo time, and TM is the 'mixing time' between the second and third 90° pulses

drive them, reducing RF power deposition in patients (measured as specific absorption rate, SAR), and permitting higher bandwidth RF pulses to be used (which is significant in the context of the chemical shift displacement artifact; see above). However, against all of these advantages, the stimulated echo of the STEAM sequence only detects a maximum of 50% of the available signal, which is why it is only used in a few niche applications.

ISIS

The ISIS[18] sequence is illustrated in Figure 6. While it also uses the intersection of slices for localization, it is not a single-shot method but requires the addition and subtraction of a series of measurements to fully localize the signal. The principle is most readily understood by considering the one dimensional case (Figure 7). Here, two scans are acquired. In the first scan (Expt. 1), signal is acquired following a nonselective excitation pulse, i.e., from the whole region within the sensitive volume

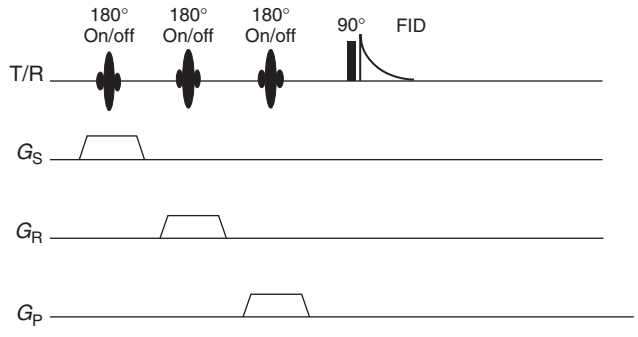

Figure 6. Timing sequence for ISIS localization in three dimensions. Signals from all on/off permutations of the slice-selective 180° RF pulses are acquired and combined, using a scheme similar to that shown in Table 1. T/R indicates radiofrequency transmit pulses and received signal; G_S, G_R, and G_P are gradients in the slice, read, and phase-encode directions, respectively

of the RF coil. All spins in the sample will have the same phase. The second scan starts with a slice-selective inversion pulse, inverting spins in the selected slice (Figure 7, top). After the 90° read pulse, these spins will have opposite phase to those outside the slice. Subtraction of the signals from the two measurements leads to addition of signal from within the slice, but subtraction or cancellation of the signal from outside.

Using eight ON/OFF combinations of three orthogonal slice-selective inversion pulses before the 90° read pulse, together with an appropriate add/subtract scheme, enables the resulting signal to be localized to a cuboid. It is only the RF pulses that are switched on and off, not the gradient pulses (G_S, G_R, and G_P in Figure 6), so that eddy current effects are the same in each measurement. However, in practice there are slight differences in signal amplitudes from different regions of the sample experiencing different numbers of inversion pulses in the different measurements, which can lead to subtraction errors. The amount of contamination depends on the ordering chosen, whether adiabatic pulses are used, and whether a postacquisition saturation pulse is used.[19,20] One optimal combination is given in Table 1. Saturating the signal outside the voxel of interest can also help reduce contamination.[21]

Contamination is minimized when the voxel of interest is relatively large compared with the sensitive volume of the RF receiver coil. This is one reason why the ISIS sequence has been more used for ^{31}P MRS for which larger volumes tend to be acquired owing to its lower sensitivity compared with ^{1}H MRS.

Table 1. An optimal ISIS ordering scheme

180_x	180_y	180_z	Add or subtract
On	Off	On	+
Off	On	Off	−
On	On	Off	+
Off	Off	On	−
On	Off	Off	−
Off	On	On	+
On	On	On	−
Off	Off	Off	+

From Ref. 19.

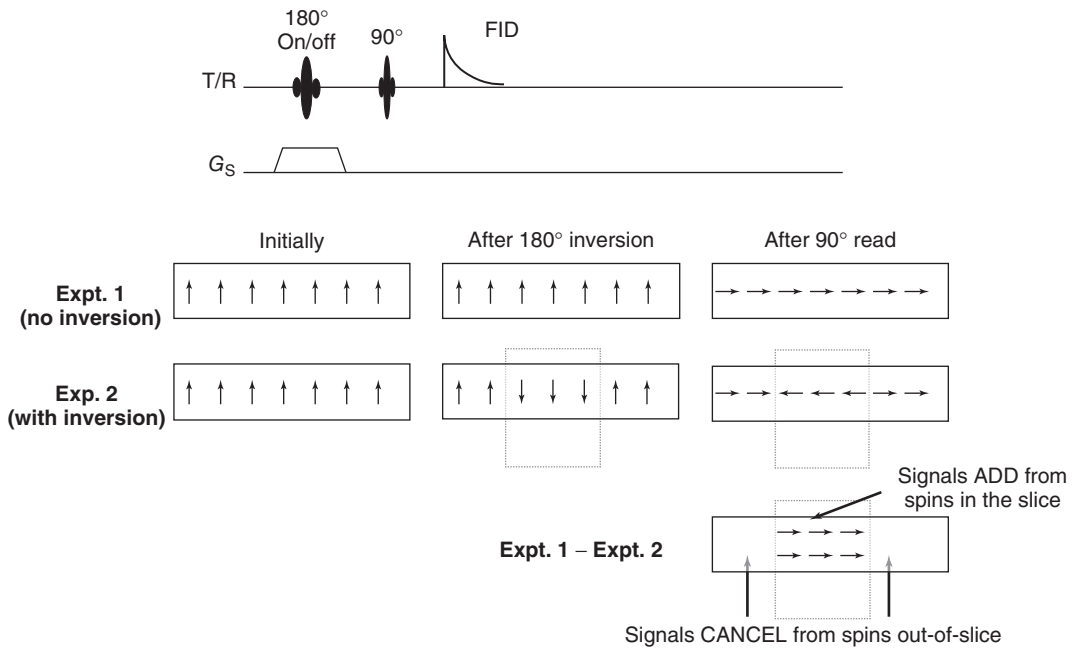

Figure 7. ISIS in one dimension. In a first measurement, the 180° RF pulse is Off, signal is acquired from the full object, and all spins are in phase (Expt. 1, center). In a second measurement, an initial 180° pulse inverts the spins in the selected slice, so that after the read pulse they have opposite phase to the spins outside the slice (Expt. 2, center). Subtraction of signals from the two measurements causes signals from spins within the slice to add coherently, while signal from spins outside the slice will cancel (bottom). T/R indicates RF pulse transmission and signal reception; G_S is the slice-select gradient

Another reason why ISIS has been used more than PRESS for ^{31}P measurements is that many metabolites of interest have a short transverse relaxation time constant (T_2), and during ISIS localization, the magnetization is primarily along $\pm z$ rather than in the transverse plane as is the case for the PRESS sequence.

An important modification to the original implementation of ISIS is the replacement of standard inversion pulses with adiabatic hyperbolic secant pulses.[8] These have two major advantages. Firstly, they have good slice profiles, leading to better edge definition of the voxel (flatter response in the middle, and no side-lobes; Figure 2). Secondly, as these RF pulses are adiabatic, they enable a good inversion of spins within the selected slice independent of the strength of the RF field (provided the RF amplitude is above a certain threshold value). This property is especially useful when transmit-receive RF surface coils are being used to optimize the signal-to-noise ratio (SNR) of the detected signals and where standard amplitude-modulated RF pulses would lead to a flip angle that depends on position relative to the RF coil. In this context, adiabatic pulses both optimize the inversion efficiency and also reduce the need for careful calibration of the RF pulses at the start of the measurement. For the same reason, an adiabatic excitation pulse can also be used for the read pulse.

LASER

The LASER[22,23] sequence is, in principle, a PRESS sequence modified for use with RF transmit–receive surface coils by the inclusion of adiabatic RF pulses. However, unlike the ISIS method, it is not possible to simply replace the amplitude-modulated pulses with adiabatic equivalents. This is because while the adiabatic pulses can produce uniform inversion across a slice, for transverse magnetization they produce a dispersal of phase, so that the spins are not refocused. It is, however, possible to use pairs of identical adiabatic inversion pulses, for which the second pulse compensates for the phase dispersal of the first.

In the original implementation of the LASER sequence, a nonselective excitation was followed by three pairs of adiabatic inversion pulses such as hyperbolic secant pulses, to obtain localization in three dimensions (Figure 8). A variant of this, known as semi-LASER, uses a slice-selective excitation instead of the nonselective excitation followed by the first pair of adiabatic RF pulses.[24] This reduces the number of RF pulses required, and also the associated RF power deposition. Neither scheme is widely available on clinical MR systems, as most clinical studies use ^{1}H MRS for which the uniform transmit field of the RF body coil makes the standard PRESS sequence entirely adequate. The only present exception is at ultrahigh magnetic field (e.g., 7 T and above) for which body transmit coils are not yet available. LASER sequences are, however, used in a preclinical research context, and in specialized research applications on clinical scanners.

A further modification to the LASER sequence is to replace adiabatic inversion pulses with pulses in which the RF amplitude and frequency and the magnetic field gradient amplitude are all modulated together, such as the GOIA[15,25] or FOCI[13,26,27] pulses. This option enables an increase in RF bandwidth of an order-of-magnitude without increasing the required peak

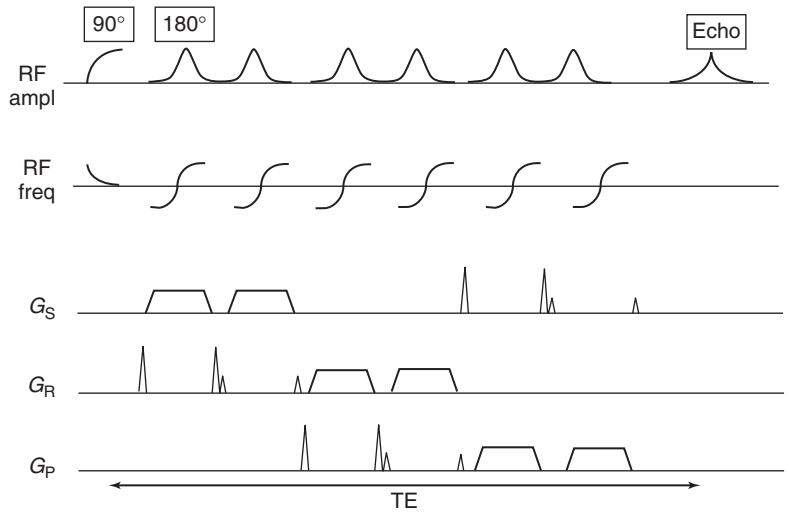

Figure 8. LASER Sequence. The initial adiabatic 90° excitation pulse is followed by three pairs of identical, slice-selective hyperbolic secant inversion (180°) pulses, which include both amplitude (top trace) and frequency (vertical axis and second trace) modulation. The phase dispersion created by the first pulse of each pair is exactly corrected by the second pulse. Signal is acquired from the cuboid corresponding to the intersection of the three slices. G_S, G_R, and G_P are the gradient amplitudes in the slice, read, and phase-encode directions. The spikes indicate short but intense gradient spoiler pulses

RF amplitude, thus reducing the chemical shift displacement artifact (see below) to negligible proportions.

Practical Considerations

Examination Overview

A typical MRS examination includes the following components, some aspects of which are described in more detail in later sections. In many protocols, most of the steps are automated and hidden to the user; however, it is important to know that they exist as often data quality can be greatly improved by optimizing them.

1. MR images, preferably in at least two orientations, are required to enable voxel positioning. When the spectroscopy sequence is added to an existing imaging protocol in which MRI contrast agents are used, their effect on MRS signal intensities must be considered (see below).
2. The spectroscopy voxel is placed on the target tissue using a graphical user interface on the scanner. A second voxel for scanner adjustments (which may include adjustment of frequency, transmitter, receiver gain, and shim currents) is typically required; this may be coincident with the target voxel but sometimes it is helpful to make it a little larger or smaller or offset, depending on the surrounding structures.
3. Adjustments are performed over this 'Adjust voxel'. Not all adjustments are required (depending on scanner architecture), but shimming is always required.
4. For ^{1}H MRS, optimization of water suppression is usually performed. Fat suppression may also be required.
5. Acquire the MRS data from the spectroscopy voxel.
6. Perform the required MRS data analysis on the scanner, and/or export it for processing in separate spectroscopy analysis packages such as jMRUI, LCModel, Tarquin, or the like (see ***Quantifying Spectra in the Frequency Domain***; ***Time-Domain Methods for Quantifying MR Spectra***).

Imaging protocols that include contrast agent injection may help identify where best to position the voxel, but they potentially affect the metabolite signal amplitudes and linewidths.[28] The effect depends on the proximity of the metabolite to the contrast agent, and also to their relative charged states.[29]

MRS Nuclei and RF Coils

For ^{1}H MRS, the standard ^{1}H imaging coils supplied with the scanner can be used (see ***Detection coils for MRS***). In most cases, this will involve the body coil for transmitting the required RF pulses and phased-array receivers for signal detection. Spectroscopy data are usually added together using standard algorithms.[30]

Other nuclei used in MRS in vivo (such as ^{31}P, ^{19}F, and ^{13}C) require dedicated hardware tuned to their appropriate Larmor frequencies. These may use the same coil element for RF transmission and signal detection, or may use coil systems with separate transmit and receive elements. As ^{1}H MR images are still required for voxel positioning, the coil systems must either be dual-resonant to permit ^{1}H operation as well, or they must be designed in such a way that they do not interfere with the standard scanner ^{1}H coils used in the same examination.

Shimming

Placing an inhomogeneous object such as a patient into a previously uniform magnetic field produces distortions in the magnetic field, especially near boundaries between tissues of different magnetic susceptibility. The resulting inhomogeneities in the magnetic field lead to broader and distorted spectral lines, poorer spectral resolution, and difficulties in achieving good water suppression. There are contributions

from macroscopic effects (for example, near air spaces) as well as microscopic changes in local susceptibility.[31] The process of shimming applies additional nonuniform magnetic fields to counteract these effects. These are usually designed to create magnetic field profiles in the form of spherical harmonics, up to second order (see ***Magnetic Resonance Spectroscopy Instrumentation***). The first-order shim coils create effectively the same magnetic field profiles as the x, y, and z MRI gradient coils, while the higher-order shims approximate gradients denoted by z^2, x^2-y^2, zx, zy, and $2xy$ terms. There is also a 'z^0' coil. The fact that it is possible to reduce spectral linewidths by adjusting the currents in these eight coils alone demonstrates that the dominant inhomogeneity often arises from macroscopic effects. However, microscopic effects also contribute, especially at higher magnetic field.[31]

As the size of a single MRS voxel is usually quite small, it is often possible to achieve much better spectral linewidths than is possible for MRSI, for which the shimmed volume may include a number of susceptibility variations and discontinuities, which can make shimming very difficult.

For many years the only way to optimize the magnetic field in the voxel was to adjust the currents iteratively in each coil and view the effect on the free induction decay (FID). As a large signal is required, this is often only feasible using ^{1}H signals from tissue water. Being an iterative process in which changes in one shim can alter the optimal value in another shim, means that it is really only practicable to optimize the linear shim currents in this way. Even exploring this restricted three-dimensional shim space, which often included local minima, requires significant time and expertise.

Fortunately, a number of algorithms have been developed to automate this process. They start with a measurement of the existing magnetic field distribution over the region of interest. Knowledge of the effects of currents in the different shim coils on the magnetic field distribution then permits the calculation of the required shim currents to minimize the inhomogeneity. It is relatively straightforward to include the higher-order shims in this process. To calculate the required corrections uses either a mapping of the magnetic field in three dimensions[32,33] or along linear projections to characterize the magnetic field in terms of spherical harmonic functions.[34,35]

Water and Fat Suppression

For most ^{1}H MRS measurements, it is desirable to reduce the large signal from tissue water. This enables better use of the scanner receiver's dynamic range for detecting the metabolites of interest, which will be present at much lower concentration. While the high bit depth of modern analogue-to-digital converters deployed in the receiver makes the acquisition of spectra without water suppression possible,[36,37] localized spectra acquired in this way tend to be contaminated by sidebands, including acoustic gradient artifacts, which are symmetric or antisymmetric signals from around the water peak[38] that can dominate metabolite resonances. As these artifacts are proportional to the size of resonance peaks, water suppression largely eliminates this problem. Water suppression also reduces the baseline distortion produced by the large wings of the water resonance, although this can also be achieved in postprocessing. Sometimes water suppression is deliberately set as incomplete, so that there is still an intense resonance peak left in the spectrum for use in frequency and phase correction (see the section titled 'Motion Effects').

A wide range of methods have been suggested to achieve selective water suppression for in vivo spectroscopy (see ***Water Suppression in Proton MRS of Humans and Animals***, ***The Basics***). Most water suppression strategies are applied before the main localization sequence. Long presaturation pulses, widely used in high-field solution-state NMR systems, are rarely used owing to the long repetition times (TR) involved and RF power delivery and deposition issues in modern scanners. They also give rise to changes in peak intensity owing to the nuclear Overhauser effect.[39] Instead, most methods use a combination of selective excitation of the water resonance, followed by a spoiler gradient. This general method is called CHESS (CHEmical Shift Selective) and was originally introduced to eliminate fat (or water) in MR images.[40,41] In standard implementations, there are two or three excitation pulses, each followed by a spoiler gradient. The RF pulses need to be quite long (e.g., 25 ms) in order to achieve the required frequency selectively and avoid disturbance to the metabolites of interest. The flip angles will be close to 90°, but usually at least one pulse will have a flip angle greater than 90° to allow for longitudinal relaxation between the water suppression and the spectral acquisition, and is likely to be adjusted empirically in each case (the efficiency of the water suppression is very sensitive to the precise flip angle used). Some specific implementations of this include the four-pulse WET (*W*ater suppression *E*nhanced through T_1 effects[42]) sequence and the seven-pulse VAPOR (*V*ariable *P*ulse power and *O*ptimized *R*elaxation delays[43]) sequence.

Spectra from some tissues are also prone to substantial contamination and distortion by intense lipid resonances. This is especially problematic when the tissue is adjacent to large lipid concentrations, such as in the brain next to the scalp, or at the edge of the prostate. Contamination from adjacent tissue occurs because the edges of selected slices used for voxel selection may not be sufficiently sharp, or the chemical shift displacement artifact may shift the selected slice into the lipid region (see the section titled 'Chemical Shift Displacement Artifact'). Although spectroscopic imaging (MRSI) does not typically have a significant chemical shift displacement artifact, MRSI does suffer from a similar (if not worse) problem of voxel bleed (see ***CSI and SENSE CSI***).

There are two main strategies to reduce this problem: the use of saturation slices with sharp edges (see below), and lipid suppression. Lipid suppression generally requires a different approach to water suppression owing to the shorter relaxation times. Some form of inversion recovery scheme before the main localization sequence is sometimes used, so that the lipid signal is nulled at the time of data acquisition, although it can be problematic to include this as well as water suppression and outer volume suppression modules. A more popular approach when using PRESS with long echo times is to use MEGA (Mescher-Garwood)[44] or BASING (band-selective inversion with gradient dephasing)[10] pulses, which are selective 180° pulses placed during the echo time of the sequence. These

cause selective dephasing of the lipid signals, while (ideally) leaving metabolites of interest unaffected. These pulses can also be used for water suppression, or combined water and lipid suppression when appropriate dual-band versions of the RF pulses are used.

Outer and Inner Volume Suppression

The slice profiles of RF pulses are not perfectly sharp, which can lead to significant contamination of signals from adjacent tissues. This is especially a concern when adjacent tissues contain a high concentration of lipid. As for a given RF waveform the transition region of slice profiles is proportional to the voxel size, the problem increases with voxel size, for example, when a single-voxel localization technique is used to limit the excited region to a fairly large volume for subsequent higher-resolution MRSI encoding. The chemical shift displacement artifact can exacerbate this effect.

One solution is to apply narrower saturation pulses around the voxel. As these are narrower they can use higher gradient strengths and therefore both the transition region and the chemical shift displacement effect are reduced. Very selective saturation (VSS) pulses have been developed to improve the performance of this approach. First developed for imaging,[45] they were soon applied to reduce contamination in spectroscopy scans.[46] They use a linear frequency sweep to spread the energy in the pulse and produce much sharper excitation profiles. Compared with a 4 ms four-lobe 90° sinc-gauss pulse, which has a transition band that is 40% of the pass band, for example, a 3 ms 90° VSS pulse has a transition band that is only 6% of the pass band.[46] To maximize the signal from the voxel, the voxel size may be increased (e.g., by 20%) and saturation slices used across the transition bands so that final signal detection is from the desired region. This method is sometimes known as Overpress.[47]

Inner volume suppression also employs saturation slices, but is used to eliminate signals from subvoxels with differing phase that may lead to signal subtraction. This situation arises when coupled spin systems (e.g., lactate) experience different numbers of refocusing pulses in different regions of the voxel.[10]

Reference Scans

^{1}H MRS protocols usually include the collection of a few transients of signal without water suppression. Given the high SNR of water, this signal is quickly acquired and provides a reference to help correct the effects of eddy currents[48]; perform frequency and phase correction of the data; and to act as an internal concentration reference (see ***Measuring Metabolite Concentrations I–Brain ^{1}H MRS***). Eddy currents are induced in metallic structures in the bore of the magnet owing to the switching of magnetic field gradients. These in turn produce an additional contribution to the magnetic field, with a time-varying decay that adds a phase term to the signal evolution and leads to distortion of the spectral peaks. As this effect also applies to the water signal, it can be used to correct for the phase effects induced by eddy currents before Fourier transformation. It also has the benefit of giving a zero-order phase correction to the data. A related technique is the QUALITY algorithm,[49] in which the metabolite signal is divided by the water signal to correct for the effects of magnetic field inhomogeneity.

Motion Effects

Tissue motion during acquisition means that spectra will be contaminated by signals from adjacent tissues that are moving in and out of the prescribed volume. In addition, individual acquisitions will vary in frequency and phase.[50] The result is a blurring of the acquisition volume and a degradation of the line shape and SNR of the metabolites.

Breath-holding is not really feasible owing to the long duration of most MRS studies, so a number of other approaches have been put forward to overcome the problems of respiratory motion.[50–54] These techniques generally fall into three categories: prospectively gated acquisitions, offline correction of phase and frequency distortions, and volume tracking. Prospectively gated acquisitions have the advantage of confining the volume of acquisition more precisely to the prescribed volume but are constrained to use the relatively long TR of the respiratory motion. In contrast, data acquired for offline correction may use a shorter TR and therefore allow more signal averages and an increased SNR per unit time. These methods rely on frequency and phase correction of each individual acquisition before coaddition using a peak with a high SNR (usually the ^{1}H signal from tissue water). This reverses the SNR loss from motion-induced dephasing and frequency blurring, improving the overall spectral SNR and narrowing the linewidth,[50,55] but it does not address the problem of different tissues moving into the voxel and causing contamination. The third class of correction methods uses measurements of tissue motion fed back to the scanner to alter the position of the localized volume and hence to track the target[56,57].

In addition to subject motion, magnetic field drift during the scan can also lead to frequency change and hence to line broadening. The heating and cooling of thermo-sensitive static magnetic shims used in the manufacture of MRI magnets, following a prior gradient-intense clinical MRI exam, is a common source of such drift.[58] While this is a particular problem in MRSI owing to the relatively small frequency bandwidth in the phase-encode directions, leading to localization errors,[59,60] it is a problem in single-voxel MRS as well.[58] Field drift will also lead to artifacts in any measurements relying on data subtraction. While use of a deuterium (^{2}H) field-frequency lock, as used in high-resolution solution-state NMR systems, is generally not feasible in the clinical context, it is possible to monitor the frequency of an intense resonance such as water and apply a correction either to the magnetic field[61] or to the frequency/phase of individual acquisitions, as described for motion correction above.[50,55] Alternatively, the frequency can be measured and a postprocessing correction can be applied.[62]

Biographical Sketch

Geoffrey S. Payne. b 1962, BA (Cantab) 1983, MSc 1984 Aberdeen, PhD 1989 Oxford. First encountered MRI in the group of Jim and Meg Hutchison in Aberdeen during his Master's degree, followed by a PhD in Oxford, UK with Professors George Radda and Peter Styles, studying multiple quantum filtering for distinguishing intracellular

vs extracellular ^{23}Na. He joined the Cancer Research UK Clinical Magnetic Resonance Research Group in Sutton, Surrey, UK in 1989. Approximately 70 papers. His main research interest is in applications of localized biomedical magnetic resonance spectroscopy (^{1}H, ^{31}P, ^{19}F, and ^{13}C) and imaging in cancer research.

Related Articles

Single Voxel Localized Proton NMR Spectroscopy of Human Brain In Vivo; Single Voxel Whole Body Phosphorus MRS; Magnetic Resonance Spectroscopy Instrumentation; Detection coils for MRS; Adiabatic RF Pulses for MRS; Quantifying Spectra in the Frequency Domain; Time-Domain Methods for Quantifying MR Spectra; Localized MRS employing RF (B1) gradient methods; CSI and SENSE CSI; Measuring Metabolite Concentrations I–Brain ^{1}H MRS

References

1. J. J. Ackerman, T. H. Grove, G. G. Wong, D. G. Gadian, and G. K. Radda, *Nature*, 1980, **283**, 167.
2. R. E. Gordon, P. E. Hanley, D. Shaw, D. G. Gadian, G. K. Radda, P. Styles, P. J. Bore, and L. Chan, *Nature*, 1980, **287**, 736.
3. P. A. Bottomley, T. B. Foster, and R. D. Darrow, *J. Magn. Reson.*, 1984, **59**, 338.
4. J. Pauly, P. Le Roux, D. Nishimura, and A. Macovski, *IEEE Trans. Med. Imaging*, 1991, **10**, 53.
5. M. Shinnar, L. Bolinger, and J. S. Leigh, *Magn. Reson. Med.*, 1989, **12**, 81.
6. M. Shinnar, S. Eleff, H. Subramanian, and J. S. Leigh, *Magn. Reson. Med.*, 1989, **12**, 74.
7. J. Mao, T. Mareci, and E. Andrew, *J. Magn. Reson.*, 1988, **79**, 1.
8. M. Silver, R. Joseph, C.-N. Chen, V. Sank, and D. Hoult, *Nature*, 1984, **310**, 681.
9. M. Silver, R. Joseph, and D. Hoult, *Phys. Rev. A*, 1985, **31**, 2753.
10. D. A. Kelley, L. L. Wald, and J. M. Star-Lack, *J. Magn. Reson. Imaging*, 1999, **9**, 732.
11. R. A. Edden, M. Schar, A. E. Hillis, and P. B. Barker, *Magn. Reson. Med.*, 2006, **56**, 912.
12. M. A. Janich, R. F. Schulte, M. Schwaiger, and S. J. Glaser, *J. Magn. Reson.*, 2011, **213**, 126.
13. R. J. Ordidge, M. Wylezinska, J. W. Hugg, E. Butterworth, and F. Franconi, *Magn. Reson. Med.*, 1996, **36**, 562.
14. S. Conolly, D. Nishimura, and A. Macovski, *J. Magn. Reson.*, 1988, **78**, 440.
15. A. Tannus and M. Garwood, *NMR Biomed.*, 1997, **10**, 423.
16. P. Bottomley, *Ann. N. Y. Acad. Sci.*, 1987, **508**, 333.
17. J. Frahm, K. D. Merboldt, and W. Hanicke, *J. Magn. Reson.*, 1987, **72**, 502.
18. R. Ordidge, A. Connelly, and J. Lohman, *J. Magn. Reson.*, 1986, **66**, 283.
19. C. Burger, R. Buchli, G. McKinnon, D. Meier, and P. Boesiger, *Magn. Reson. Med.*, 1992, **26**, 218.
20. G. B. Matson, D. J. Meyerhoff, T. J. Lawry, R. S. Lara, J. Duijn, R. F. Deicken, and M. W. Weiner, *NMR Biomed.*, 1993, **6**, 215.
21. A. Connelly, C. Counsell, J. A. B. Lohman, and R. J. Ordidge, *J. Magn. Reson.*, 1988, **78**, 519.
22. J. Slotboom and W. M. M. J. Bovee, *Concepts Magnetic Res.*, 1995, **7**, 193.
23. M. Garwood and L. DelaBarre, *J. Magn. Reson.*, 2001, **153**, 155.
24. T. W. Scheenen, D. W. Klomp, J. P. Wijnen, and A. Heerschap, *Magn. Reson. Med.*, 2008, **59**, 1.
25. J. Near, C. Romagnoli, A. T. Curtis, L. M. Klassen, J. Izawa, J. Chin, and R. Bartha, *J. Magn. Reson. Imaging*, 2009, **30**, 335.
26. P. Kinchesh and R. J. Ordidge, *J. Magn. Reson.*, 2005, **175**, 30.
27. C. S. Arteaga de Castro, V. O. Boer, A. Andreychenko, J. P. Wijnen, U. A. van der Heide, P. R. Luijten, and D. W. Klomp, *NMR Biomed.*, 2013, **26**, 1213.
28. P. E. Sijens, M. J. van den Bent, P. J. Nowak, P. van Dijk, and M. Oudkerk, *Magn. Reson. Med.*, 1997, **37**, 222.
29. P. S. Murphy, A. S. Dzik-Jurasz, M. O. Leach, and I. J. Rowland, *Magn. Reson. Imaging*, 2002, **20**, 127.
30. S. M. Wright and L. L. Wald, *NMR Biomed.*, 1997, **10**, 394.
31. R. Gruetter, S. A. Weisdorf, V. Rajanayagan, M. Terpstra, H. Merkle, C. L. Truwit, M. Garwood, S. L. Nyberg, and K. Ugurbil, *J. Magn. Reson.*, 1998, **135**, 260.
32. P. Webb and A. Macovski, *Magn. Reson. Med.*, 1991, **20**, 113.
33. E. Schneider and G. Glover, *Magn. Reson. Med.*, 1991, **18**, 335.
34. R. Gruetter, *Magn. Reson. Med.*, 1993, **29**, 804.
35. R. Gruetter and C. Boesch, *J. Magn. Reson.*, 1992, **96**, 323.
36. D. B. Clayton, M. A. Elliott, and R. E. Lenkinski, *Concepts Magnetic Res.*, 2001, **13**, 260.
37. J. W. van Der Veen, D. R. Weinberger, G. Tedeschi, J. A. Frank, and J. H. Duyn, *Radiology*, 2000, **217**, 296.
38. D. Clayton, M. Elliot, J. Leigh, and R. Lenkinski, *J. Magn. Reson.*, 2001, **153**, 203.
39. J.-H. Chen, E. B. Sambol, P. T. Kennealey, R. B. O'Connor, P. L. DeCarolis, D. G. Cory, and S. Singer, *J. Magn. Reson.*, 2004, **171**, 143.
40. P. A. Bottomley, T. H. Foster, and W. M. Leue, *Proc. Natl. Acad. Sci. U. S. A.*, 1984, **81**, 6856.
41. A. Haase, J. Frahm, W. Hanicke, and D. Matthaei, *Phys. Med. Biol.*, 1985, **30**, 341.
42. R. J. Ogg, P. B. Kingsley, and J. S. Taylor, *J. Magn. Reson. Ser. A*, 1994, **104**, 1.
43. I. Tkac, Z. Starcuk, I. Y. Choi, and R. Gruetter, *Magn. Reson. Med.*, 1999, **41**, 649.
44. M. Mescher, A. Tannus, M. O'Neil Johnson, and M. Garwood, *J. Magn. Reson. Ser. A*, 1996, **123**, 226.
45. P. Le Roux, R. J. Gilles, G. C. McKinnon, and P. G. Carlier, *J. Magn. Reson. Imaging*, 1998, **8**, 1022.
46. T. K. Tran, D. B. Vigneron, N. Sailasuta, J. Tropp, P. Le Roux, J. Kurhanewicz, S. Nelson, and R. Hurd, *Magn. Reson. Med.*, 2000, **43**, 23.
47. Y. Li, J. A. Osorio, E. Ozturk-Isik, A. P. Chen, D. Xu, J. C. Crane, S. Cha, S. Chang, M. S. Berger, D. B. Vigneron, and S. J. Nelson, *Magn. Reson. Imaging*, 2006, **24**, 1295.
48. U. Klose, *Magn. Reson. Med.*, 1990, **14**, 26.
49. A. A. de Graaf, J. E. van Dijk, and W. M. Bovee, *Magn. Reson. Med.*, 1990, **13**, 343.
50. G. Helms and A. Piringer, *Magn. Reson. Med.*, 2001, **46**, 395.
51. S. M. Noworolski, P. C. Tien, R. Merriman, D. B. Vigneron, and A. Qayyum, *Magn. Reson. Imaging*, 2009, **27**, 570.
52. J. M. Lin, S. Y. Tsai, H. S. Liu, H. W. Chung, R. V. Mulkern, C. M. Cheng, T. C. Yeh, and N. K. Chen, *Magn. Reson. Med.*, 2009, **62**, 1394.
53. R. W. van der Meer, J. Doornbos, S. Kozerke, M. Schar, J. J. Bax, S. Hammer, J. W. Smit, J. A. Romijn, M. Diamant, L. J. Rijzewijk, A. de Roos, and H. J. Lamb, *Radiology*, 2007, **245**, 251.
54. J. Star-Lack, E. Adalsteinsson, G. Gold, D. Ikeda, and D. Spielman, *Magn. Reson. Med.*, 2000, **43**, 325.

55. R. E. Gabr, S. Sathyanarayana, M. Schar, R. G. Weiss, and P. A. Bottomley, *Magn. Reson. Med.*, 2006, **56**, 754.
56. S. Kozerke, M. Schar, H. J. Lamb, and P. Boesiger, *Magn. Reson. Med.*, 2002, **48**, 380.
57. B. Keating, W. Deng, J. C. Roddey, N. White, A. Dale, V. A. Stenger, and T. Ernst, *Magn. Reson. Med.*, 2010, **64**, 672.
58. A. M. El-Sharkawy, M. Schar, P. A. Bottomley, and E. Atalar, *MAGMA*, 2006, **19**, 223.
59. A. Tal and O. Gonen, *Magn. Reson. Med.*, 2013, **70**, 895.
60. O. Schmidt, S. Widmaier, M. Bunse, W. I. Jung, G. J. Dietze, and O. Lutz, *MAGMA*, 2000, **10**, 167.
61. P. G. Henry, P. F. van de Moortele, E. Giacomini, A. Nauerth, and G. Bloch, *Magn. Reson. Med.*, 1999, **42**, 636.
62. M. Zaitsev, O. Speck, J. Hennig, and M. Buchert, *NMR Biomed.*, 2010, **23**, 325.

Further Reading

R. A. de Graaf, In vivo NMR Spectroscopy: Principles and Techniques, 2nd edn, Wiley: Chichester, 2007.